INTERNATIONAL JOURNAL FOR NUMERICAL METHODS IN FLUIDS
Int. J. Numer. Meth. Fluids **29**: 575–585 (1999)

COMPUTATION OF UNSTEADY TRANSONIC FLOW OVER A FIGHTER WING USING A ZONAL NAVIER–STOKES/FULL-POTENTIAL METHOD

OLYMPIO ACHILLES de FARIA MELLO[a,*] AND LAKSHMI N. SANKAR[b]

[a] *Instituto de Aeronáutica e Espaço, Centro Técnico Aeroespacial 12228-904, São José dos Campos, Brazil*
[b] *School of Aerospace Engineering, Georgia Institute of Technology, Atlanta, GA 30332, USA*

SUMMARY

An improved hybrid method for computing unsteady compressible viscous flows is presented. This method divides the computational domain into two zones. In the inner zone, the Navier–Stokes equations are solved using a diagonal form of an alternating-direction implicit (ADI) approximate factorisation procedure. In the outer zone, the unsteady full-potential equation (FPE) is solved. The two zones are tightly coupled so that steady and unsteady flows may be efficiently solved. Characteristic-based viscous/inviscid interface boundary conditions are employed to avoid spurious reflections at that interface. The resulting CPU times are about 60% of the full Navier–Stokes CPU times for unsteady flows in non-vector processing machines. Applications of the method are presented for a F-5 wing in steady and unsteady transonic flows. Steady surface pressures are in very good agreement with experimental data and are essentially identical to the full Navier–Stokes predictions. Density contours show that shocks cross the viscous/inviscid interface smoothly, so that the accuracy of full Navier–Stokes equations can be retained with significant savings in computational time. Copyright © 1999 John Wiley & Sons, Ltd.

KEY WORDS: transonic flow; zonal methods; viscous/inviscid interaction; unsteady flow; finite difference methods

1. INTRODUCTION

Transonic flow is characterised by the presence of regions of supersonic flow embedded in a subsonic region. Mathematically, the governing equations are inherently non-linear, a fact that has prevented the application of traditional analytical tools and early numerical methods to the analysis of such a flow condition. In addition, transonic flows tend to be more unsteady and three-dimensional than purely subsonic and supersonic flows [1].

In non-steady flow situations, the presence of a supersonic region embedded in a subsonic region causes downstream disturbances to be propagated upstream with a considerable time lag, which results in significant out-of-phase forces. It has been known for quite some time [2] that transonic flow conditions are critical for flutter, with the flutter dynamic pressure being substantially reduced for Mach numbers near unity, in a phenomenon that has been called 'transonic dip' [3]. The severity of flutter at transonic speeds is linked to the presence of moving shock waves over the wing surface [4]. From these considerations, it is clear that

* Correspondence to: Instituto de Aeronáutica e Espaço, Centro Técnico Aeroespacial, 12228-904, São José dos Campos, Brazil.

CCC 0271–2091/99/050575–11$17.50
Copyright © 1999 John Wiley & Sons, Ltd.
Received January 1998
Revised April 1998

accurate flutter predictions depend on the ability of the computational fluid dynamics procedure to predict correct shock strength and location, in a time-accurate fashion.

Transonic small disturbance equation (TSD) and full-potential equation (FPE) based methods have been extensively used to compute complex configurations. These methods, in some cases, have been coupled to interactive boundary layer analyses to allow solution of problems where viscous effects can be included in a limited way.

For problems where substantial separation occurs, the TSD and FPE techniques coupled with interactive boundary layer analysis are not adequate, since the concept of a boundary layer is no longer applicable. For these cases, Navier–Stokes methods are clearly needed. However, these are still computationally expensive and have seen limited practical use for complete configurations due to this factor. This becomes especially evident for problems where extensive computations are needed, such as the prediction of transonic flutter [3].

The present method is an extension of the work initiated by Sankar *et al.* [5], who developed a zonal Navier–Stokes/full-potential method. The approach used here is to solve the FPE in an outer zone, away from solid surfaces and viscous regions, and solve the Navier–Stokes equations in an inner zone, where viscous effects are essential. This approach is schematically illustrated in Figure 1. This results in a highly efficient solver that retains the accuracy of the Navier–Stokes methodology near the solid surface, and the simplicity of a potential flow solver away from solid surfaces.

The mathematical formulation used here is described in detail elsewhere [6] and only a brief outline is presented next.

2. NAVIER–STOKES FORMULATION

The Navier–Stokes solver used in the present work was developed by Sankar *et al.* [7]. The vector form of the full Reynolds-averaged, 3D Navier–Stokes equations based on an arbitrary curvilinear co-ordinate system can be written in non-dimensional form as:

$$\boldsymbol{Q}_\tau + \boldsymbol{E}_\xi + \boldsymbol{F}_\eta + \boldsymbol{G}_\zeta = \frac{1}{Re}(\boldsymbol{R}_\xi + \boldsymbol{S}_\eta + \boldsymbol{T}_\zeta), \tag{1}$$

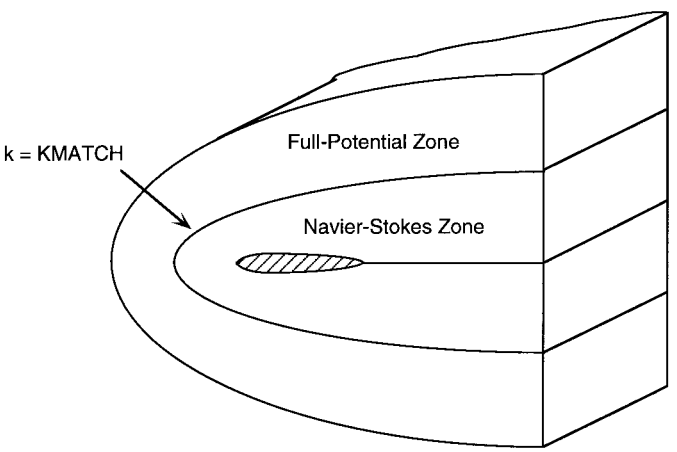

Figure 1. Partitioning of computational domain into inner and outer zones.

Copyright © 1999 John Wiley & Sons, Ltd.

where $\boldsymbol{Q}$ is the vector of unknown flow properties; $\boldsymbol{E}$, $\boldsymbol{F}$ and $\boldsymbol{G}$ are the inviscid flux vectors; $\boldsymbol{R}$, $\boldsymbol{S}$ and $\boldsymbol{T}$ are the viscous flux vectors and $Re = \rho_\infty a_\infty c/\mu_\infty$ is the Reynolds number based on the free stream speed of sound a_∞, density ρ_∞, viscosity μ_∞, and reference chord c.

The time derivative, $\boldsymbol{Q}_\tau$, of Equation (1) is approximated using two-point backward difference at the new time level $n+1$. All spatial derivatives are approximated by standard second-order central differences and are represented by the difference operators δ. The streamwise and normal derivatives, $\boldsymbol{E}_\xi$ and $\boldsymbol{G}_\zeta$, are evaluated implicitly at the new time level $n+1$. The spanwise derivative, $\boldsymbol{F}_\eta$, is evaluated explicitly at the old time level n but uses the $n+1$ values as soon as they become available. This semi-explicit treatment of the spanwise derivative enables the scheme to solve implicitly for $\Delta\boldsymbol{Q}^{n+1}$ at all points at a given spanwise station at a time. To eliminate any dependency the solution may have on the sweeping direction, the solver reverses the direction of spanwise sweeping with every sweep.

The viscous terms $\boldsymbol{R}_\xi$, $\boldsymbol{S}_\eta$ and $\boldsymbol{T}_\zeta$ are evaluated explicitly, using half-point central differences denoted here by the difference operator $\bar{\delta}$, so that the computational stencil for the stress terms uses only three nodes in each of the three directions. Explicit treatment of the stress terms still permits the use of large time steps since the Reynolds numbers of interest here are fairly large.

With the above described time and space discretisations, Equation (1) becomes:

$$\Delta\boldsymbol{Q}^{n+1} + \Delta\tau(\delta_\xi \boldsymbol{E}^{n+1} + \delta_\eta \boldsymbol{F}^{n,n+1} + \delta_\zeta \boldsymbol{G}^{n+1}) = \frac{\Delta\tau}{Re}(\bar{\delta}_\xi \boldsymbol{R}^{n,n+1} + \bar{\delta}_\eta \boldsymbol{S}^{n,n+1} + \bar{\delta}_\zeta \boldsymbol{T}^{n,n+1}). \quad (2)$$

Application of Equation (2) to the grid points leads to a system of non-linear, block pentadiagonal matrix equations for the unknown $\Delta\boldsymbol{Q}^{n+1} = \boldsymbol{Q}^{n+1} - \boldsymbol{Q}^n$, Equation (2), since the convection fluxes $\boldsymbol{E}$, $\boldsymbol{F}$ and $\boldsymbol{G}$ are non-linear functions of the vector of unknown flow properties $\boldsymbol{Q}$. Equation (2) is then linearised using the Jacobian matrices $\mathbf{A} = \partial\boldsymbol{E}/\partial\boldsymbol{Q}$ and $\mathbf{C} = \partial\boldsymbol{G}/\partial\boldsymbol{Q}$. This results in a system of linear, block pentadiagonal matrix equations, which is considerably expensive to solve. The approach used here is to employ an approximate factorisation and the diagonal algorithm of Pulliam and Chaussee [8], to diagonalise $\mathbf{A}$ and $\mathbf{C}$. This approach yields:

$$\boldsymbol{T}_\xi^n[\mathbf{I} + \Delta\tau\delta_\xi \Lambda_\xi^n]\mathbf{N}^n[\mathbf{I} + \Delta\tau\delta_\zeta \Lambda_\zeta^n](\boldsymbol{T}_\zeta^{-1})^n \Delta\boldsymbol{Q}^{n+1} = \mathrm{RHS}^{n,n+1}. \quad (3)$$

The solution of Equation (3) involves two block tridiagonal systems where the blocks are diagonal matrices.

The use of standard central differences to approximate the spatial derivatives can give rise to the growth of high frequency errors in the numerical solution with time. To control this growth, a set of second-/fourth-order non-linear, spectral radius based, explicit artificial dissipation terms are added to the discretised equations.

A slightly modified version of the Baldwin–Lomax algebraic turbulence model is used, where the maximum shear stress is used instead of the wall shear stress because in the vicinity of separation points, the shear stress values approach zero at the wall.

3. FULL-POTENTIAL FORMULATION

The full-potential solver used in the present work was developed by Sankar *et al.* [9]. The 3D unsteady compressible potential flow equation, in a body-fitted co-ordinate system, may be written as a second-order hyperbolic partial differential equation for the perturbation potential φ:

Copyright © 1999 John Wiley & Sons, Ltd.

$$\frac{\rho}{a^2 J}\left[\varphi_{\tau\tau} + U\varphi_{\xi\tau} + V\varphi_{\eta\tau} + W\varphi_{\zeta\tau}\right] = \left(\frac{\rho U}{J}\right)_{\xi} + \left(\frac{\rho V}{J}\right)_{\eta} + \left(\frac{\rho W}{J}\right)_{\zeta}, \tag{4}$$

where ρ is the density; U, V and W are the contravariant components of velocity and J is the Jacobian of the transformation between Cartesian and curvilinear co-ordinates.

At a given time level n, the disturbance velocity potential φ and its temporal derivative φ_τ are known, and consequently all velocity components, speed of sound and density are also known. Equation (4) is a partial differential equation for φ with non-linear coefficients. To circumvent the non-linearities, the coefficients ρ, a^2, J, U, V and W appearing on the left-hand-side, and the density ρ appearing on the right-hand-side of Equation (4) are computed at the time level n. The remaining quantities in (4) are kept at the new time level $n+1$. In the process of evaluating the contravariant velocities U, V and W, two-point central differences are used to evaluate the derivatives of φ and the transformation metrics at the grid points and locations mid-distance between the grid points.

The temporal derivatives on the left-hand-side of Equation (4) are discretised using two-point backward finite difference operators. The mixed space–time derivatives appearing in (4) are discretised using two-point upwind-differencing for the spatial derivative, and two-point backward-differencing for the temporal derivative. The flux-like terms appearing on the right-hand-side of (4) are evaluated using two-point central-difference formulas with half intervals, using the density ρ computed at the time level n, while the contravariant components of velocity are computed using mixed information from time level n and the new time level $n+1$, in order to reduce the number of diagonals in the final matrix of coefficients.

In order to maintain numerical stability in regions of supersonic flow, the numerical formulation must be constructed in such a way that it is consistent with the physical domain of dependence. For that purpose, the artificial compressibility method is used. Here, the density values ρ that appear in $(\rho U/J)$ on the right-hand-side of Equation (4) are biased in the direction of the flow.

When the above discretisations are employed, at each grid point a linear equation results for the change in the solution in two consecutive time steps $\Delta\varphi^{n+1} = \varphi^{n+1} - \varphi^n$. Application of this linear equation at the grid points result in a sparse pentadiagonal matrix system that may be expressed as:

$$[M]\{\Delta\varphi\}^{n+1} = \{R\}^n. \tag{5}$$

The matrix $[M]$ is approximately factored as the product of two sparse lower ($[L]$) and upper ($[U]$) matrices each having four diagonals, with their elements recursively related to the coefficients of the matrix $[M]$. The solution to Equation (5) is then obtained using a two-step procedure.

4. NAVIER–STOKES/FULL-POTENTIAL COUPLING

A typical partitioning of the domain into an inner zone and an outer zone is illustrated in Figure 1. The plane $k = \mathrm{KMATCH}$ corresponds to the interface between the inner zone and the outer zone. Previous applications of the hybrid NS/FPE solver to an iced wing configuration showed an oscillatory behaviour in convergence histories that indicated false reflections from the Navier–Stokes/full-potential interface. Similar numerical phenomena were observed in the past with respect to far-field boundary conditions: Acoustic waves travelled from the solid surface to the outer boundary and were reflected back to contaminate the solution and delay convergence [10]. The spurious waves responsible for the oscillatory convergence

Copyright © 1999 John Wiley & Sons, Ltd.

behaviour need to be eliminated. In unsteady flows this is even more important since these spurious waves will compromise the time accuracy of the solution.

Non-reflecting far-field boundary conditions would not be directly applicable to the viscous/inviscid interface discussed here because perturbations in one zone must be transmitted to the other zone. The disturbances in the inner region should contribute to the outgoing waves only, while the disturbances in the outer region should contribute to the ingoing waves only, so that there is no reflection at the interface.

Following a development analogous to Giles' derivation of approximate non-reflecting boundary conditions [11], a set of characteristics $\mathbf{c}$ normal to a $\zeta = \text{constant}$ surface was obtained. These characteristics were related to small perturbations on the primitive variables. The resulting characteristic equations are integrated according to the signs of the corresponding eigenvalues. This corresponds to the eigenvalue splitting $\Lambda_\zeta = \Lambda_\zeta^+ + \Lambda_\zeta^-$ and corresponding characteristic splitting $\mathbf{c} = \mathbf{c}^+ + \mathbf{c}^-$:

$$\mathbf{c}_\tau^+ + \Lambda_\zeta^+ \mathbf{c}_\zeta^+ = 0\,, \qquad \mathbf{c}_\tau^- + \Lambda_\zeta^- \mathbf{c}_\zeta^- = 0. \tag{6}$$

For the Navier–Stokes solver, the vector $\boldsymbol{Q}$ at the viscous/inviscid interface is updated using the characteristics obtained from the integration of Equation (6). For the full-potential solver, two of the characteristics are expressed in terms of the Riemann invariants, which are computed according to the signs of the corresponding eigenvalues. The flow properties at the interface are then updated from the Riemann invariants.

The above procedure has been successful in suppressing the oscillatory behaviour observed in previous version of the hybrid method. Although the procedure is strictly valid only for steady flows [6], it was used also for unsteady flows with results similar to those obtained by full Navier–Stokes computations.

5. RESULTS AND DISCUSSION

In the present work, the F-5 wing in transonic flow undergoing pitch oscillations was investigated. This is a very rigorous test for the present method, due to the development of shock waves that cross the viscous/inviscid interface. The interface boundary conditions are therefore required to propagate significant disturbances. In the unsteady flow simulations, these disturbances have to be propagated in a time-accurate fashion, which presents an even more rigorous test. The experimental results used here were obtained by Tijdeman *et al.* [12] who measured steady and time-dependent pressures at eight spanwise stations.

The computational grid used in the present study is illustrated in Figure 2. The Navier–Stokes and full-potential solvers were interfaced so that about half of the number of points were located in each zone.

5.1. Steady flow simulations

Steady pressure coefficient ($C_P = 2p/\rho_\infty V_\infty^2$) distributions for $M = 0.95$, zero angle of attack, at spanwise stations 35.2, 72.1 and 97.7% are shown in Figure 3. Here the dominating feature is the shock that forms over most of the wing, on both upper and lower surfaces. The upper surface shock is stronger and aft of the lower surface shock. These features were well-predicted by the current method. The suction peaks and location of matching upper and lower surface pressures are again well-predicted, except at the station 97.7%, where the experimental data indicate a lower suction peak. This test case was demanding in the sense that the shock crosses

Copyright © 1999 John Wiley & Sons, Ltd.

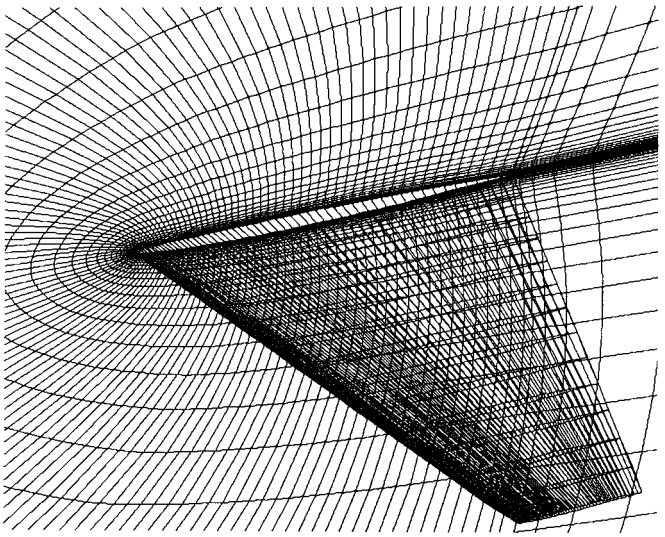

Figure 2. Computational grid for the F-5 wing.

the Navier–Stokes/full-potential interface, and the results presented here indicate that the hybrid method is able to predict adequately both shock location and strength even when the discontinuities due to the shock are propagated through the Navier–Stokes/full-potential interface. Further evidence to support this conclusion is presented in Figure 4, where the density contours at station 81.7% of span are shown. In this figure, the Navier–Stokes/full-potential interface is drawn to facilitate the analysis. It can be seen that the contours smoothly cross the interface, and in particular the shock is well-captured across the interface.

The results presented here show that the hybrid method can be successfully applied to steady transonic flows, even when the shock crosses the Navier–Stokes/full-potential interface. The differences between the computed and measured data are of the same order of, or lower than, the more costly Navier–Stokes solutions presented by other researchers [13].

5.2. Unsteady Flow Simulations

Unsteady transonic flows are very challenging to the present method, due to the presence of strong disturbances generated by unsteady shock motion, which need to be propagated through the Navier–Stokes/full-potential interface in a time-accurate fashion.

For the unsteady flow simulations presented here, the Mach number was 0.95. The wing was in pitching oscillations with a frequency of 40 Hz about half-chord, and around $\alpha_0 = 0°$.

Under these pitching oscillations, the F-5 wing deforms aeroelastically. During the investigation reported by Tijdeman *et al.* [12], the wing vibration mode was measured for the various test runs using eight accelerometers. These measurements were used to obtain an approximate analytical expression for the vertical wing displacement at various points, assuming no chordwise deformation (rigid rotation) and parabolic spanwise deformation. This approximation to the elastic deformation allows a consistent representation by a rigid rotation about the node corresponding to each spanwise station. The nodal line corresponding to the case presented here is illustrated in Figure 5, from Tijdeman *et al.* [12].

The non-dimensional time step was 0.005. An additional computation to assess the effect of the time step was made with a non-dimensional time step of 0.002. The real and imaginary

Copyright © 1999 John Wiley & Sons, Ltd.

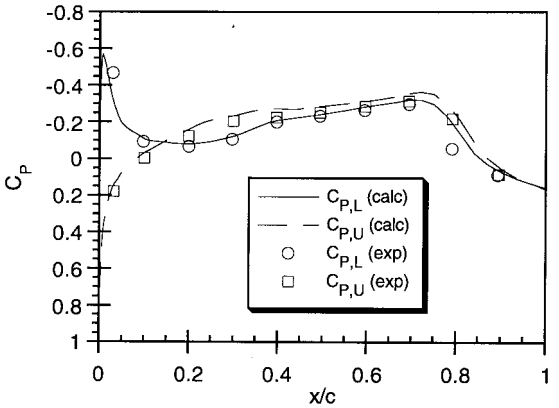

(a) 35.2% Span

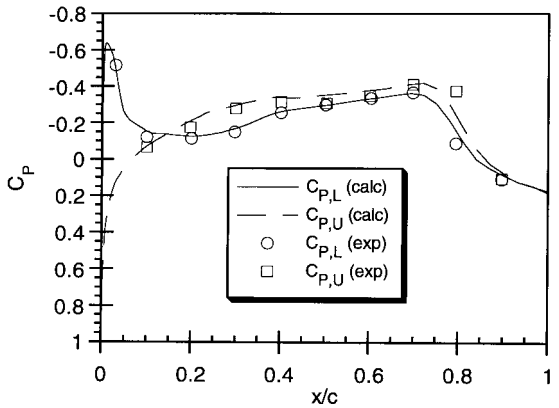

(b) 72.1% Span

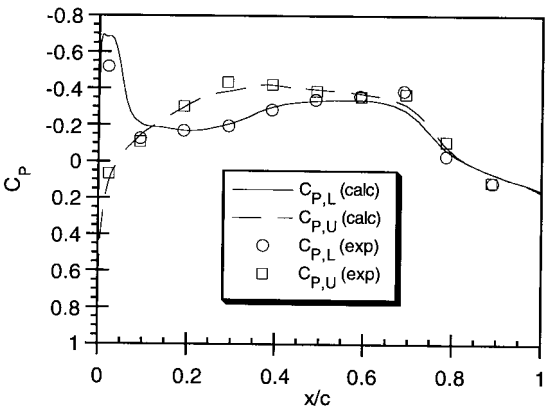

(c) 97.7% Span

Figure 3. Steady surface pressure distributions, $M = 0.95$.

Copyright © 1999 John Wiley & Sons, Ltd.

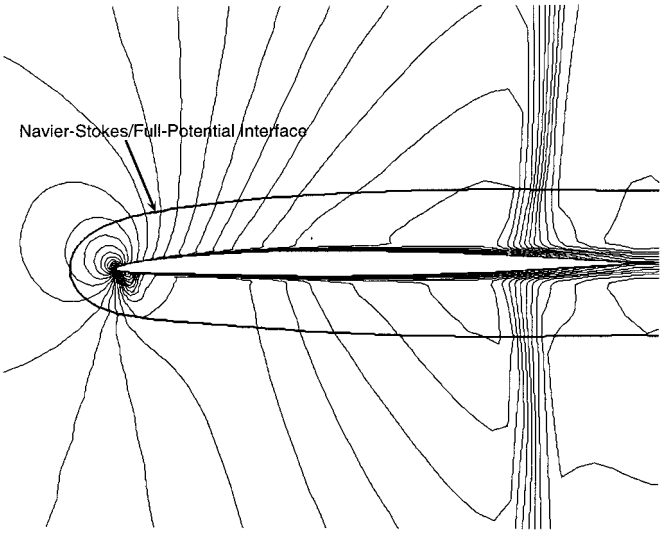

Figure 4. Density contours at 81.7% span, $M = 0.95$.

parts of the unsteady pressure coefficient distributions at spanwise stations 35.2, 72. 1 and 97.7% are shown in Figure 6. As occurred in the previous test case, at all spanwise stations, strong leading edge peaks are present in the lower surface both in the in-phase and out-of-phase component and they seem to be well-predicted by the present method. The steady flow results, shown in Figure 3, indicate a strong shock on both upper and lower surfaces around 80% of the chord. The experimental data for the unsteady case, seen in Figure 6, show significant peaks around this chordwise location, mostly in the real (in-phase) component, but also in the imaginary (out-of-phase) component. These peaks are very localised, which indicates that they result more from shock strength variations than shock movement. The numerical results presented in Figure 6 show that the present method was unable to correctly predict the peak in the real part, but predicted the peak in the imaginary part. The computations with a smaller time step show some improvement in the real part, which indicate that the time step might have to be further reduced to yield a better correlation. Further reductions in time step were not attempted because of the large CPU resources that would be needed. It should also be noted that the current coarse grid presents some smearing in the shock, therefore small changes in the shock strength are not likely to be well-captured, even with a smaller time step.

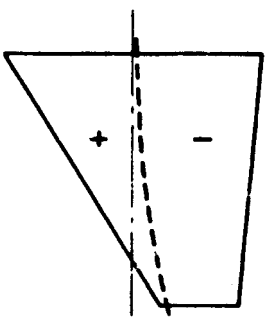

Figure 5. Nodal line.

Copyright © 1999 John Wiley & Sons, Ltd.

Except for the above discussed discrepancy, the unsteady pressure coefficient distribution is well-predicted. It should be noted that this is a very rigorous test for the present method, due to the strong shock crossing the Navier–Stokes interface, as seen in Figure 4. The results presented here indicate that the discrepancies observed in this test case are inherent to the Navier–Stokes module, and can probably be overcome by using an upwind Navier–Stokes module capable of capturing sharper shocks.

Overall, the unsteady pressure coefficient distributions correlate well with experimental data and are similar to those obtained with equivalent full Navier–Stokes computations, with a fraction of the computational cost. The savings in CPU time were found to depend on the vector capability of the CPU, ranging from 27% on the Cray Y/MP-L up to 40% on a HP Apollo 730 workstation.

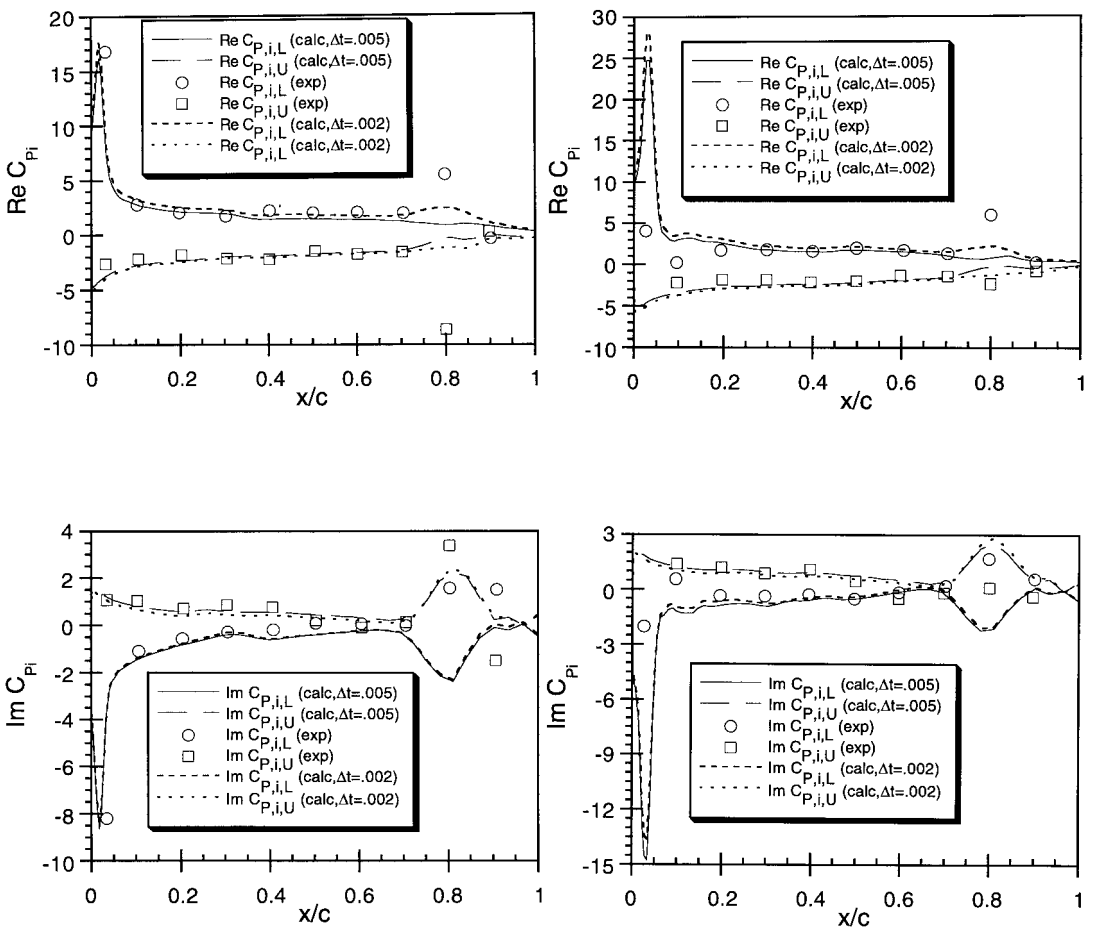

(a) 35.2% Span

(b) 72.1% Span

Figure 6. Unsteady surface pressure distributions, $M = 0.95$, $f = 40$ Hz.

Copyright © 1999 John Wiley & Sons, Ltd.

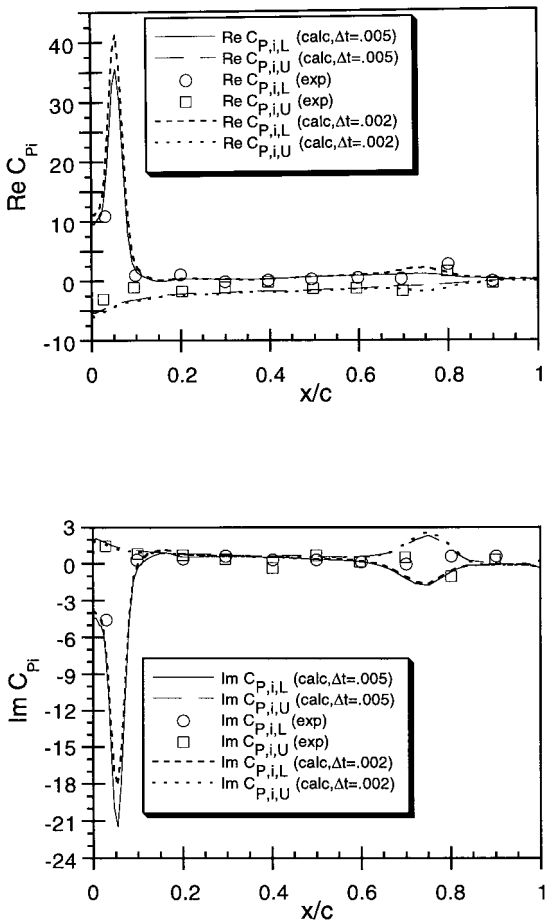

(c) 97.7% Span

Figure 6 (*Continued*)

6. CONCLUSION

An improved hybrid Navier–Stokes/full-potential method has been successfully applied to transonic steady and unsteady flow around an F-5 fighter wing. It was found that the present technique allowed flow parameters to change smoothly across the viscous/inviscid interface. Pressure coefficient distributions agreed very well with experimental data. It should be noted that the shocks considered here have been virtually normal to the Navier–Stokes/full-potential interface. For this reason, further investigations should be carried out before applying the present method to flow situations where significantly oblique shocks are present.

For the computations presented here, the two zones had the same number of grid points. With this configuration, the savings in total CPU time were found to depend on the vector capability of the CPU, ranging from 27% on the Cray Y/MP-L up to 40% on a HP Apollo 730 workstation. For steady flow cases, the computational savings were slightly higher, because the hybrid method presented convergence rates higher than the full Navier–Stokes method.

Copyright © 1999 John Wiley & Sons, Ltd.

The location of the viscid/inviscid interface is a major factor in determining the actual savings for practical applications. For problems where massive separation occurs, this interface would have to be located farther away from solid surfaces, with a larger number of points in the inner zone. For these cases, the savings in CPU times would be reduced and might not be significant enough to justify the use of the present method. For problems where little or no separation occurs, the interface can be located closer to solid surfaces, so that less than half of the grid points would be located in the inner zone, and the computational savings could be increased even further. For helicopter rotor blades, dynamic partitioning between the viscous and inviscid domains [14] allows optimal computational savings.

The present hybrid technique, which combines the accuracy of Navier–Stokes methods in the viscous regions with the economy of potential flow methods in inviscid regions, may be used as a stepping stone for more ambitious efforts involving aeroelastic and unsteady aerodynamic analysis of complete aircraft configurations.

ACKNOWLEDGMENTS

O.A. de F.M. was supported by the Conselho Nacional de Desenvolvimento Científico e Tecnológico (CNPq) and the Fundação de Amparo àPesquisa do Estado de São Paulo (FAPESP), Brazil.

REFERENCES

1. W.F. Ballhaus, 'Some recent progress in transonic flow computations', in H.J. Wirz and J.J. Smolderen (eds.) *Numerical Methods in Fluid Dynamics*, Hemisphere Publishing, Washington, DC, 1978.
2. M.T. Landahl, *Unsteady Transonic Flow*, Pergamon, New York, 1951.
3. W. Whitlow Jr., 'Computational unsteady aerodynamics for aeroelastic analysis', *NASA TM-100523*, 1987.
4. H. Ashley, 'Role of shocks in the 'sub-transonic' flutter phenomenon', *J. Aircraft*, **17**, 187 (1980).
5. L.N. Sankar, B.K. Bharadvaj and F.-L. Tsung, 'A three-dimensional Navier–Stokes/full-potential coupled analysis for viscous transonic flow', *AIAA J.*, **31**, 1857–1862 (1993).
6. O.A.F. Mello, 'An improved hybrid Navier–Stokes/full-potential method for computation of unsteady compressible viscous flows', *Ph.D. Dissertation*, Georgia Institute of Technology, Atlanta, GA, 1994.
7. L.N. Sankar and O.J. Kwon, 'High-alpha simulation of fighter aircraft', *Proc. NASA High Angle-of-Attack Technology Conference*, Vol. 1, NASA CP-3149, Pt. 2, NASA Langley Research Center, Hampton, VA, 1990, pp. 689–702.
8. T.H. Pulliam and D.S. Chaussee, 'A diagonal form of an implicit approximate factorization algorithm', *J. Comput. Phys.*, **39**, 347–363 (1981).
9. L.N. Sankar, J.B. Malone and Y. Tassa, 'An implicit conservative algorithm for steady and unsteady three-dimensional transonic potential flows', *AIAA Paper 811016*. Proc. AIAA 5th Computational Fluid Dynamics Conference, Palo Alto, CA, 1981, pp. 199–212.
10. K. Mazaheri and P.L. Roe, 'New light on numerical boundary conditions', *AIAA Paper 91-1600-CP*, AIAA 10th Computational Fluid Dynamics Conference, Honolulu, Hawaii, 1991.
11. M. Giles, 'Nonreflecting boundary conditions for Euler equation calculations', *AIAA J.*, **28**, 2050–2058 (1990).
12. H. Tijdeman, J.W.G. van Nunen, A.N. Kraan, A.J. Persoon, R. Poestkoke, R. Roos, P. Schippers and C.M. Siebert, 'Transonic wind tunnel tests on an oscillating wing with external stores, Part II: clean wing', *Air Force Flight Dynamics Laboratory*, *AFFDL-TR-78-194*, *Part II*, Wright-Patterson AFB, OH, 1979. (Also NLR-TR-78106U, Part II).
13. S. Obayashi, G.P. Guruswamy and P.M. Goorjian, 'Streamwise upwind algorithm for computing unsteady transonic flows past oscillating wings', *AIAA J.*, **29**, 1668–1677 (1991).
14. C. Berezin, 'A coupled Navier–Stokes/full-potential analysis for rotors', *Ph.D. Dissertation*, Georgia Institute of Technology, Atlanta, GA, 1995.

Copyright © 1999 John Wiley & Sons, Ltd.